Electronic Supplementary Information (ESI)

Phenol is a pH-activated linker to gold surfaces: a single molecule conductance study

Brent Lawson[a], Hannah Skipper[b], Maria Kamenetska[a,b]

[a]Department of Physics, Boston University, Boston, Massachusetts, 02215, United States
[b]Department of Chemistry, Boston University, Boston, Massachusetts, 02215, United States

Table of Contents

I.   Sample Preparation and Aqueous STMBJ Measurements

All aqueous solutions are prepared by initially dissolving sodium hydroxide (NaOH) in MilliQ water (purchased from Sigma Aldrich) until pH 12 is reached. The molecule of interest is then dissolved to a concentration of 0.1 mM in the pH 12 solution. The pH of the solution was then checked and adjusted back to 12 if necessary. A drop of the solution is deposited on gold coated (~150 nm, prepared by thermal evaporation) substrates and dried in a low temperature oven (less than 55 °C) for ~10 minutes, leaving the molecule deposited on the surface of the Au substrate. Single molecule conductance measurements of 4-(aminomethyl)phenol ($NH_2C_1PhO^-$), 4-(2-aminoethyl)phenol ($NH_2C_2PhO^-$), 4-(3-aminopropyl)phenol ($NH_2C_3PhO^-$), and 4-(4-aminobutyl)phenol ($NH_2C_4PhO^-$) are performed. Measurements of $NH_2C_1PhO^-$, $NH_2C_2PhO^-$, $NH_2C_3PhO^-$, $NH_2C_4PhO^-$ are also shown in **Fig. S1-S4** at different junction biases, to determine if there is any bias dependence.

For measurements in aqueous solvent, the STM tip is coated in Apiezon wax.[1] Measurements in aqueous conditions, shown in **Fig. S5**, give identical results to measurements with molecules dried out of solution which are shown in the manuscript. The inability of the amine linker group to bind to Au in pH 7 aqueous conditions is shown in **Fig. S6** using 1,4-benzenediamine as an example. Additionally, in **Fig. S6**, the conductance of a diamine 4-aminobenzylamine measured in TCB is also included. The backbone of this molecule is identical to that of $NH_2C_1PhO^-$ and is included as a control to demonstrate the similarity in binding probability and persistence between phenol and amine-terminated molecules.

The junction persistence lengths as well as junction formation probabilities for $NH_2C_1PhO^-$, $NH_2C_2PhO^-$, $NH_2C_3PhO^-$, $NH_2C_4PhO^-$, are shown in **Fig. S7**. The junction probability measurements in the inset are constructed using previously reported methods.[2,3] The persistence

length distributions in the figure are generated from the 2D histograms in **Fig. 2 (e-h)** as described previously.[3] Briefly, we take vertical slices of the 2D histograms at each extension. The resulting slice conductance histogram is fit with a Gaussian fit and the peak maximum is plotted as a data point to the corresponding extension. By scanning through every extension and extracting the Gaussian fit amplitude, we achieve the distributions in **Fig. S7**. The persistence length quoted in the manuscript corresponds to the point at which the 2D feature amplitude decreases to 15% of the maximum and represents the ~longest extensions observed for a given molecule.
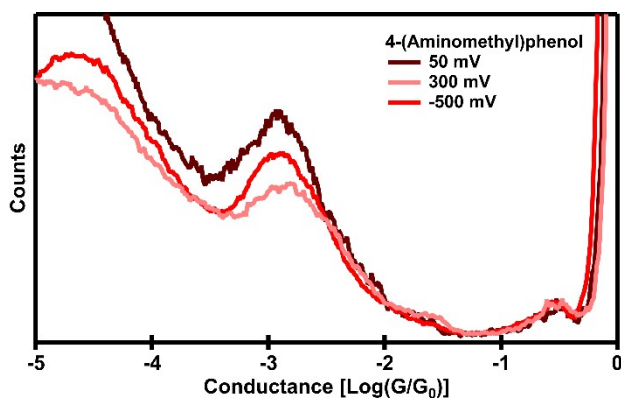
Figure S1. Conductance histogram of $NH_2C_1PhO^-$ at different junction biases.
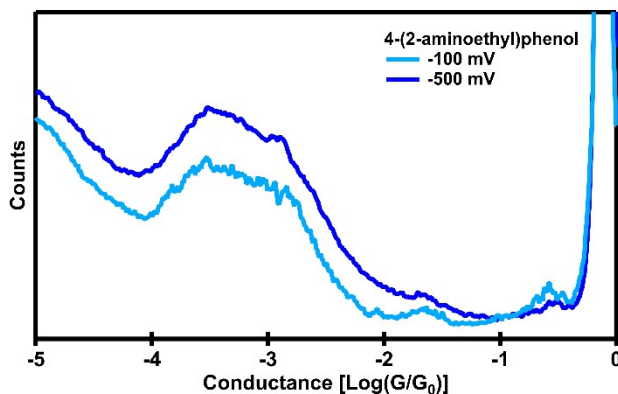
Figure S2. Conductance histogram of $NH_2C_2PhO^-$ at different junction biases.
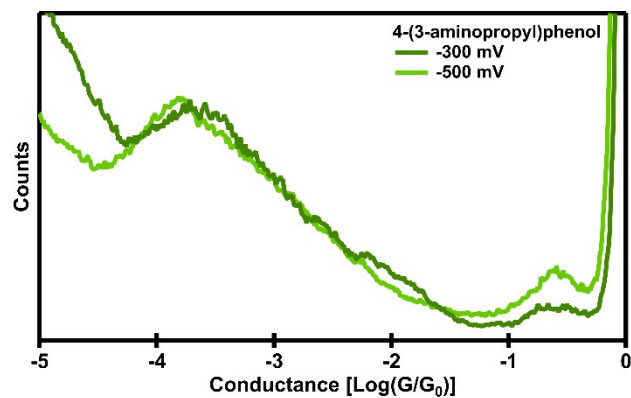
Figure S3. Conductance histogram of $NH_2C_3PhO^-$ at different junction biases.
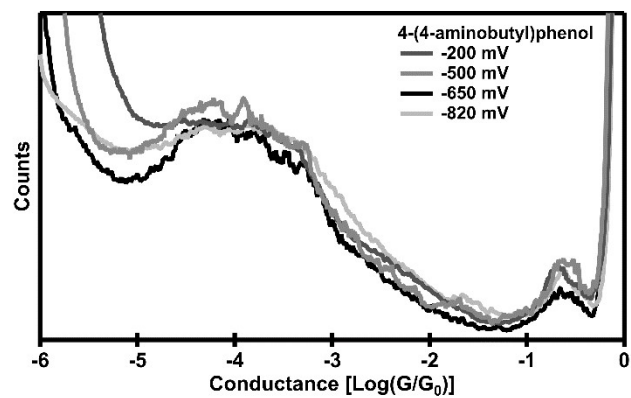
Figure S4. Conductance histogram of $NH_2C_4PhO^-$ at different junction biases.
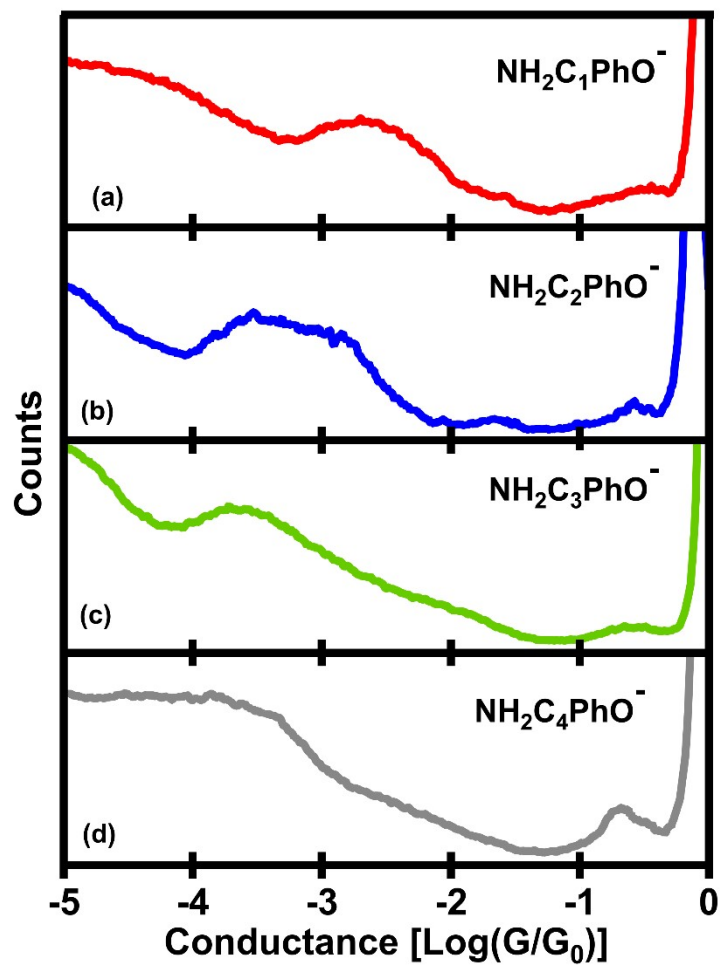
Figure S5. Conductance histograms of $NH_2C_1PhO^-$, $NH_2C_2PhO^-$, $NH_2C_3PhO^-$, and $NH_2C_4PhO^-$ constructed from at least 5000 STMBJ traces collected in aqueous pH 12 conditions with a wax-coated tip at 500 mV bias.
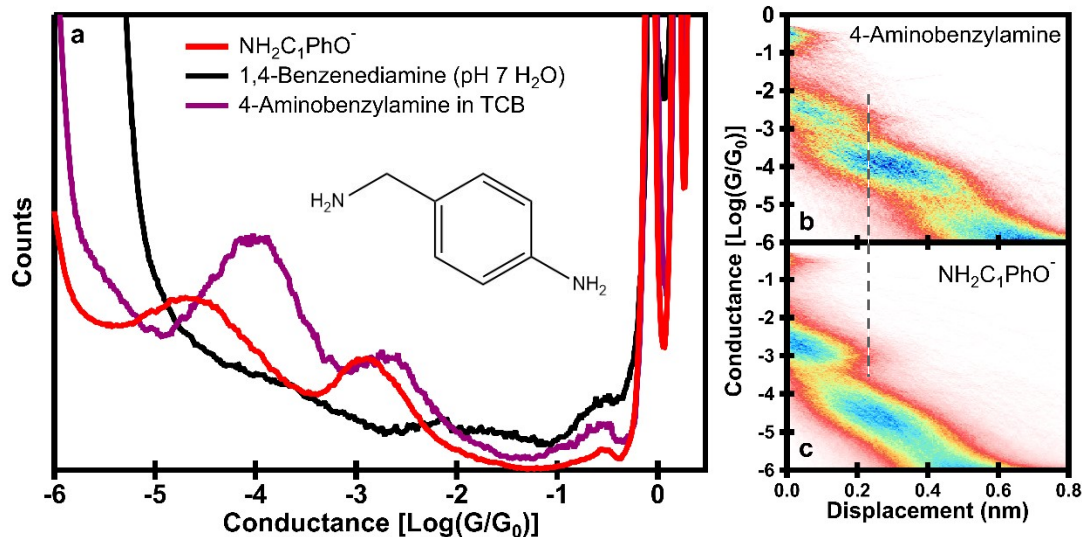
Figure S6. (a) Conductance histogram of 1 mM 1,4-benzenediamine in pH 7 H_2O with a wax coated Au tip (black), 1.5 mM 4-aminobenzylamine in TCB (maroon) and $NH_2C_1PhO^-$ in pH 12 H_2O (red). The structure of 4-aminobenzylamine is shown in the inset. **(b, c)** Conductance vs. displacement histogram of 4-aminobenzylamine and $NH_2C_1PhO^-$. The dashed vertical line emphasizes the similar persistence of the two molecules with identical backbones but differing linkers.
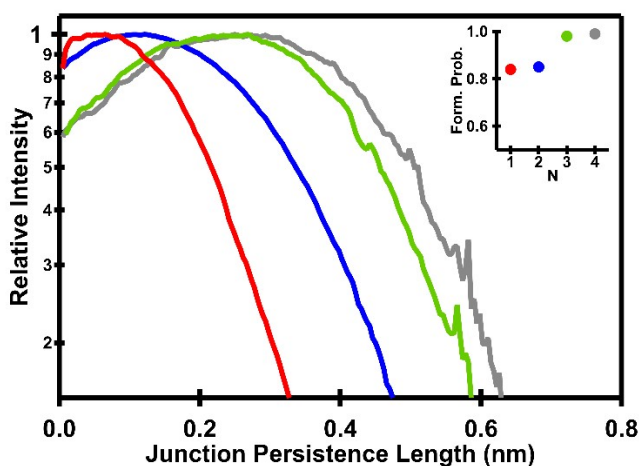
Figure S7. Junction persistence lengths of $NH_2C_1PhO^-$ (red), $NH_2C_2PhO^-$ (blue), $NH_2C_3PhO^-$ (green), and $NH_2C_4PhO^-$ (gray). Reported persistence lengths in the manuscript are calculated as the length at which the relative number of traces reaches 15% of the number at the peak of the distribution. This value is the intercept of each trace with the x-axis on this figure. The inset shows the calculated junction formation fraction for each molecule.

II. DFT+Σ Calculations

DFT+Σ adjustments on the HOMO resonance in the transmission curves for $NH_2C_1PhO^-$, $NH_2C_2PhO^-$, $NH_2C_3PhO^-$, and $NH_2C_4PhO^-$ are based on previously established methods.[4–7] The total DFT+Σ correction ($\Delta\Sigma$) comes from the addition of a gas-phase correction (Δ_1) and image charge correction (Δ_2).

$$\Delta\Sigma = \Delta_1 + \Delta_2$$

The gas-phase correction term adjusts the calculated HOMO energy eigenvalue of the gas-phase molecule based on either experimentally measured values or on calculations using more accurate methods. The image charge correction comes from adjustments of energy levels based on the interaction of a charge distribution with a conducting surface (analogous to an image charge effect). A description of the methods used to calculate both terms is given below.

To calculate Δ_1 we determine the HOMO energy level of the gas phase deprotonated molecules by an Ionization Potential calculation,

$$E_{HOMO} = - IP = E_{N-1} - E_N$$

where E_{N-1} is the total energy of the gas phase molecule with one less electron (N-1), and E_N is the total energy of the gas phase molecule. In our case, the gas phase molecule is an anion, and the ionized gas phase molecule is neutral. All geometry relaxation and energy calculations are performed using GAUSSIAN 16 and the PBE exchange-correlation functional.[8,9] Since the molecules are negatively charged, all calculations were done with the Karlsruhe Def2 basis set including diffuse corrections.[10,11] The calculated E_{HOMO} for all molecules is checked for basis-set convergence using Def2-SVPD, Def2-TZVPD, and Def2-QZVPD, with all final values reported with the Def2-QZVPD basis set. Δ_1 was then able to be determined from the difference between E_{HOMO} and the HOMO energy eigenvalue (ε_{HOMO}) of the gas phase molecules from FHI-aims (used for transport calculations). The values of E_{HOMO}, ε_{HOMO}, and Δ_1 are shown in **Table S1**.

Table S1. Calculated gas phase correction, Δ_1, used for DFT+Σ for $NH_2C_1PhO^-$, $NH_2C_2PhO^-$, $NH_2C_3PhO^-$, and $NH_2C_4PhO^-$. The calculated HOMO energy levels from Ionization Potential calculations (E_{HOMO}) and the HOMO energy eigenvalue from KS-DFT (ε_{HOMO}) are also shown.

Molecule	E_{HOMO} (eV)	ε_{HOMO} (eV)	Δ_1 (eV)
$NH_2C_1PhO^-$	-2.27	0.19	-2.46
$NH_2C_2PhO^-$	-2.17	0.29	-2.47
$NH_2C_3PhO^-$	-2.16	0.30	-2.46

$NH_2C_4PhO^-$	-2.17	0.30	-2.46

The image charge correction, Δ_2, is calculated from the relaxed molecular junction geometries. Since the molecules in the junction are anions, leading to neutral molecules when ionized, the typical practice of using a point charge in the center of the molecule to calculate the image charge offset was not applicable. Instead, the charge distribution of the neutral molecule was treated as a partial point charge on each atom (q_i), determined by a Mulliken charge calculation on the gas-phase neutral molecule in GAUSSIAN using PBE and Def2-SVP. The equation for Δ_2 is given by

$$\Delta_2 = \sum_i^M \frac{|q_i|^2}{4(z_i - z_{top})} + \sum_i^M \frac{|q_i|^2}{4(z_i - z_{bottom})}$$

where i is summed over all the atoms, and $z_i - z_{top}$ ($z_i - z_{bottom}$) is the distance from the atom to 1.75 Å above the plane of three Au atoms behind the apex Au atom on the top (bottom) electrode.[5,12,13] The calculated values of Δ_2 for the molecules studied are shown in **Table S2**.

Table S2. Calculated values for the image-charge correction term, Δ_2, for $NH_2C_1PhO^-$, $NH_2C_2PhO^-$, $NH_2C_3PhO^-$, and $NH_2C_4PhO^-$.

Molecule	Δ_2 (eV)
$NH_2C_1PhO^-$	1.1
$NH_2C_2PhO^-$	1.14
$NH_2C_3PhO^-$	1.17
$NH_2C_4PhO^-$	1.21

From the calculated values of Δ_1 and Δ_2 we calculate the total DFT+Σ correction for the HOMO energy level ($\Delta\Sigma$) as shown in **Table S3**.

Table S3. Calculated total DFT+Σ correction ($\Delta\Sigma$) from Δ_1 and Δ_2.

Molecule	Δ_1 (eV)	Δ_2 (eV)	$\Delta\Sigma$ (eV)
$NH_2C_1PhO^-$	-2.46	1.1	-1.36
$NH_2C_2PhO^-$	-2.47	1.14	-1.33
$NH_2C_3PhO^-$	-2.46	1.17	-1.29
$NH_2C_4PhO^-$	-2.46	1.21	-1.26

We then fit the HOMO transmission resonance calculated from NEGF with a Lorentzian distribution,

$$f(x) = A\frac{\gamma^2}{(x - \epsilon_0)^2 + \gamma^2}$$

where A is the Lorentzian amplitude, γ is the Lorentzian width and ϵ_0 is the resonance peak position. The adjustment made with DFT+Σ only shifts the position of the Lorentzian peak by the calculated values of $\Delta\Sigma$, leaving the other parameters fixed. The total transmission spectra calculated with KS-DFT followed by NEGF transmission calculations for MePhO-, EtPHO-, PrPhO-, and BuPhO- are shown in **Fig. S7** (also shown in the inset in **Fig. 4b**).
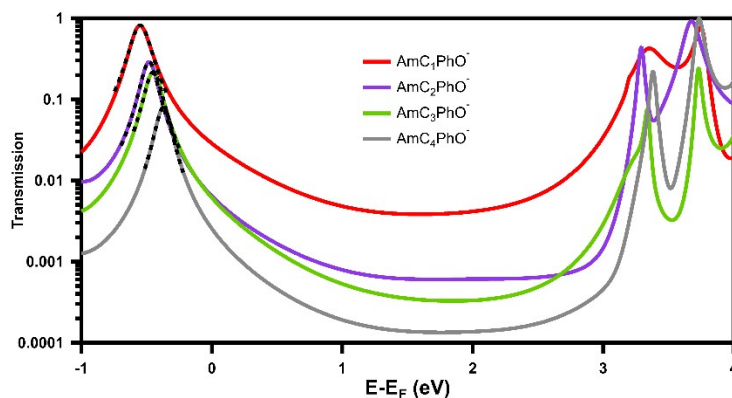
Figure S8. Transmission spectra for $NH_2C_1PhO^-$, $NH_2C_2PhO^-$, $NH_2C_3PhO^-$, and $NH_2C_4PhO^-$ calculated from KS-DFT and NEGF. Lorentzian fits for the HOMO resonances are shown by the dotted black lines.

The parameters determined from the Lorentzian fits in **Fig. S7** are shown in **Table S4.** The $\Delta\Sigma$ correction is subtracted from ϵ_0, shifting the HOMO resonance away from E_F, and yielding the final DFT+Σ corrected HOMO resonance energy (ϵ_Σ). These resonance energies are shown in **Table S4** and are used to calculate transmission in **Fig. 4b**.

Table S4. Lorentzian Fitting parameters from the NEGF transmission spectra as well as the DFT+ Σ corrected HOMO resonance energy (ϵ_Σ).

Molecule	A	γ (eV)	ϵ_0 (eV)	ϵ_Σ (eV)
$NH_2C_1PhO^-$	0.82	0.08	-0.55	-1.91
$NH_2C_2PhO^-$	0.28	0.07	-0.49	-1.82
$NH_2C_3PhO^-$	0.22	0.07	-0.45	-1.74

NH$_2$C$_4$PhO$^-$	0.08	0.07	-0.37	-1.63

III. Molecule and Molecular Junction Geometries

The molecular geometries of NH$_2$C$_1$PhO$^-$, NH$_2$C$_2$PhO$^-$, NH$_2$C$_3$PhO$^-$, and NH$_2$C$_4$PhO$^-$ and corresponding O-N distances are shown in **Table S5**. All the geometries are relaxed using FHI-AIMS with PBE functional and the tight basis set for all atoms.[14–16]

Table S5. Molecular geometry of NH$_2$C$_1$PhO$^-$, NH$_2$C$_2$PhO$^-$, NH$_2$C$_3$PhO$^-$, and NH$_2$C$_4$PhO$^-$ with their corresponding O-N distance.

Molecule	Geometry	O-N Distance (Å)
NH$_2$C$_1$PhO$^-$		6.5
NH$_2$C$_2$PhO$^-$		7.9
NH$_2$C$_3$PhO$^-$		8.9
NH$_2$C$_4$PhO$^-$		10.3
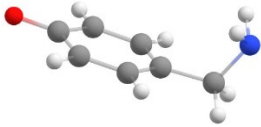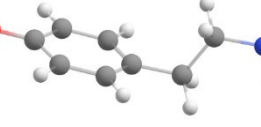
The relaxed molecular junction geometries for NH$_2$C$_1$PhO$^-$, NH$_2$C$_2$PhO$^-$, NH$_2$C$_3$PhO$^-$, and NH$_2$C$_4$PhO$^-$ bound to two Au electrodes are shown in **Table S6**. The geometries were calculated using FHI-AIMS with the PBE functional and a "tight" basis set for all atoms associated with the molecule and "loose" basis set for the Au atoms. Only the four apex Au atoms on each electrode as well as the molecular atoms were allowed to move during relaxation.

Table S6. Geometry of NH$_2$C$_1$PhO$^-$, NH$_2$C$_2$PhO$^-$, NH$_2$C$_3$PhO$^-$, and NH$_2$C$_4$PhO$^-$ bound to Au electrodes used for transmission calculations with their corresponding Au-Au distance calculated from the center of the apex Au atoms.

Molecule	Geometry	Au–Au Edge to Edge Distance (Å)

NH$_2$C$_1$PhO$^-$		7.6
NH$_2$C$_2$PhO$^-$		8.6
NH$_2$C$_3$PhO$^-$		10.1
NH$_2$C$_4$PhO$^-$		11.0

IV. Morse Potential Geometries and Calculations

The bond energy and Morse Potential calculations are performed with the molecules bound to a single Au$_{34}$ electrode. Like the junction geometry calculations, all atoms associated with the molecule and the four apex Au atoms are allowed to move to determine the initial lowest energy binding geometry. Following the initial geometry relaxation, a single Self-Consistent Field Energy calculation is done varying the Au-X (X = O, S) bond length between 1.5 and 7 Å. The relaxed geometries of the molecules discussed in **Fig. 5** and used for the Morse Potential fits are shown in **Table S7**.

Table S7. Relaxed geometries of the molecules discussed in **Fig. 5** bound to a single Au$_{34}$ electrode used for Morse Potential fitting and binding energy calculations.

Molecule	Geometry
PhO⁻	
PhOH	
$(CH_2)_2S^-$	
$(CH_2)_2SH$	
$(CH_2)_2O^-$	
$(CH_2)_2OH$	

Additional calculations are performed to distinguish any difference in the binding energy of an alkyl thiol [-$(CH_2)_2SH$ & -$(CH_2)_2S^-$], a thiophenol [-PhSH & -PhS⁻], and a thioanisole [-PhSMe] with a Au₃₄ electrode. The geometries of the different thiols binding to Au are shown in **Table S8**. While **Fig. 5** shows a significant difference between alcohol and phenol binding to Au (~0.7 eV), the difference between alkyl thiol and thiophenol binding to Au is much less (~0.3 eV) as shown in **Fig. S8** and quantified in **Table S9.**

Table S8. Relaxed geometries of protonated and deprotonated alkyl thiols and thiophenols bound to a Au₃₄ electrode used for the Bond Energy calculations in **Fig. S8**.

Molecule	Geometry
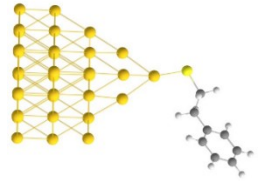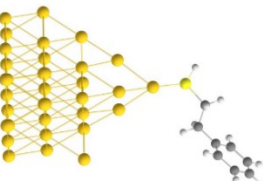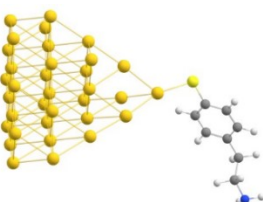
-$(CH_2)_2S^-$	
-$(CH_2)_2SH$	
-PhS^-	
-PhSH	
-PhSMe	
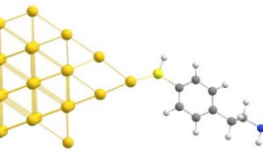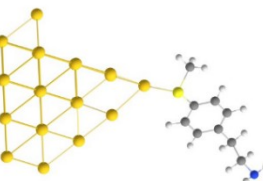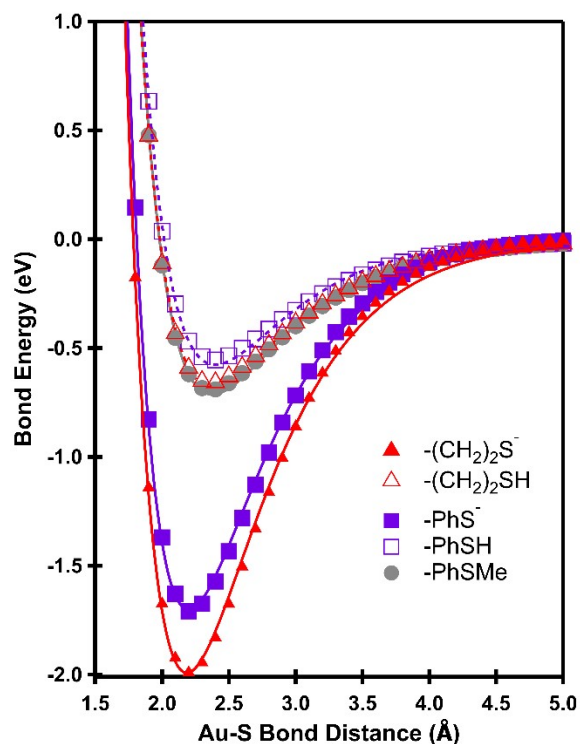
Figure S9. Potential Energy scan of the Au-S bond with molecules terminated by -(CH$_2$)$_2$SH, -(CH$_2$)$_2$S$^-$, -PhSH, -PhS$^-$, and -PhSMe. Data points were fit with a Morse Potential Fitting function.

Table S9. Morse Potential fitting parameters obtained from **Fig. S8**.

	Bond	D$_e$ (eV)	R$_e$ (Å)	a (eV)
———	-(CH$_2$)$_2$S$^-$	2.0	2.2	1.7
— – — ·	-(CH$_2$)$_2$SH	0.7	2.3	1.9
———	-PhS$^-$	1.7	2.2	1.8
— – — ·	-PhSH	0.6	2.4	1.9
———	-PhSMe	0.7	2.4	1.8

V.   References

1   L. A. Nagahara, T. Thundat and S. M. Lindsay, *Rev. Sci. Instrum.*, 1989, **60**, 3128–3130.

2   M. Kamenetska, M. Koentopp, A. C. Whalley, Y. S. Park, M. L. Steigerwald, C. Nuckolls, M. S. Hybertsen and L. Venkataraman, *Phys. Rev. Lett.*, 2009, **102**, 126803.

3   J. McNeely, N. Miller, X. Pan, B. Lawson and M. Kamenetska, *J. Phys. Chem. C*, 2020, **124**, 13427–13433.

4   S. Y. Quek, L. Venkataraman, H. J. Choi, S. G. Louie, M. S. Hybertsen and J. B. Neaton, *Nano Lett.*, 2007, **7**, 3477–3482.

5   J. B. Neaton, M. S. Hybertsen and S. G. Louie, *Phys. Rev. Lett.*, , DOI:10.1103/PhysRevLett.97.216405.

6   T. Markussen, C. Jin and K. S. Thygesen, *Phys. Status Solidi Basic Res.*, 2013, **250**, 2394–2402.

7   J. R. Widawsky, P. Darancet, J. B. Neaton and L. Venkataraman, *Nano Lett.*, 2012, **12**, 354–358.

8   D. J. Frisch, M. J.; Trucks, G. W.; Schlegel, H. B.; Scuseria, G. E.; Robb, M. A.; Cheeseman, J. R.; Scalmani, G.; Barone, V.; Petersson, G. A.; Nakatsuji, H.; Li, X.; Caricato, M.; Marenich, A. V.; Bloino, J.; Janesko, B. G.; Gomperts, R.; Mennucci, B.; Hratch, 2016.

9   J. P. Perdew, K. Burke and M. Ernzerhof, *Phys. Rev. Lett.*, 1996, **77**, 3865–3868.

10   F. Weigend, F. Furche and R. Ahlrichs, *J. Chem. Phys.*, 2003, **119**, 12753–12762.

11   D. Rappoport and F. Furche, *J. Chem. Phys.*, 2010, **133**, 134105.

12   E. Montes and H. Vázquez, *Appl. Sci.*, 2021, **11**, 1–12.

13   N. V. Smith, C. T. Chen and M. Weinert, *Phys. Rev. B*, 1989, **40**, 7565–7573.

14   A. Arnold, F. Weigend and F. Evers, *J. Chem. Phys.*, , DOI:10.1063/1.2716664.

15   A. Bagrets, *J. Chem. Theory Comput.*, 2013, **9**, 2801–2815.

16   J. Wilhelm, M. Walz, M. Stendel, A. Bagrets and F. Evers, *Phys. Chem. Chem. Phys.*, 2013, **15**, 6684–6690.